Nano Energy 72 (2020) 104687

Contents lists available at ScienceDirect

Nano Energy

journal homepage: http://www.elsevier.com/locate/nanoen

Machine learning-optimized Tamm emitter for high-performance thermophotovoltaic system with detailed balance analysis

Run Hu [a,*,1], Jinlin Song [a,1], Yida Liu [a], Wang Xi [a], Yiting Zhao [a], Xingjian Yu [a], Qiang Cheng [a], Guangming Tao [b,**], Xiaobing Luo [a,***]

[a] State Key Laboratory of Coal Combustion, School of Energy and Power Engineering, Huazhong University of Science and Technology, Wuhan, 430074, China
[b] Wuhan National Laboratory for Optoelectronics, School of Optical and Electronic Information, Huazhong University of Science and Technology, Wuhan, 430074, China

ARTICLE INFO

Keywords:
Thermophotovoltaics
Tamm emitter
Machine learning
Material informatics
Optimization

ABSTRACT

Light-matter interaction upon nanophotonic structures in the infrared wavelength has drew increasing attentions due to the extensive potential applications. Among them, thermophotovoltaic (TPV) systems can exhibit higher efficiency over the Shockley-Queisser limit due to the nanophotonic structure-enabled tunable narrowband thermal emission rather than the broadband incident spectrum. However, two long-standing issues remain formidable as bottlenecks for achieving better performances of TPV system. One is the competing role of the power density and the system efficiency of TPV system, and the other is the magnanimity possibilities of structures, configurations, dimensions, and materials of thermal emitters that disables the manual optimization of TPV system. Here, we attempt to achieve high-performance TPV system by employing the machine learning algorithm under the framework of material informatics. The power density and system efficiency are well modelled through the detailed balance analysis with full considering the photocurrent generation in the PV cells. Through optimization, the non-trial aperiodic Tamm emitters are obtained and the metal-side one is preferable in terms of the TPV performance. The present work is demonstrated to be feasible and efficient in optimizing the TPV performance, and opens a new door for the optimization problems in other fields.

1. Introduction

Tailoring thermal emission by light-matter interactions upon nanophotonic structures has been promising in a broad scope of applications, ranging from thermal management, radiative cooling, thermal camouflage, biosensing, to thermophotovoltaic (TPV) [1–16]. As the counterpart of conventional solar photovoltaic (SPV) applications, TPV systems can improve the Shockley-Queisser (SQ) limit of SPV systems by replacing the relatively broad solar spectrum with well-designed narrowband thermal emission [17]. In a SPV system, only the solar photon energy above the bandgap of a PV cell can be absorbed to separate the electron-hole pairs for photocurrent generation regardless of other energy loss and thermalization. While in a TPV system, a thermal emitter in contact with an absorber is used as the source of thermal photons rather than the non-adjustable solar photons, on which nanophotonic structures can be well designed to shift emission spectrum above the bandgap, thus allowing significant improvement in photocurrent generation [18]. Nanophotonic structures show great potential to tune thermal emission by utilizing the surface plasmons/phonon polaritons (SPPs), magnetic polaritons (MPs), hyperbolic modes and so on [19–27]. The SPPs-based emitters tend to have sharp emission peaks, while the localized SPPs -based emitters tend to have strong and broad emission peaks with *Q*-factor around 10. The combination of SPPs and localized SPPs seems to compromise the problems, but it is rather challenging in the material selection and manufacturing. Moreover, they suffer from the reliable maintenance of structure and performance. In contrast, the 1D-multilayer Tamm plasmon polaritons (TPPs) have shown superiority in both scalable manufacturing and adjustable performance as thermal emitters. TPPs are surface waves at the interface between a metallic mirror and a distributed Bragg reflector (DBR) with a zero in-plane wave vector, enabling it to be excited by incident light with in-plane wavevector less than the free space wavevector and hence

* Corresponding author.
** Corresponding author.
*** Corresponding author.
E-mail addresses: hurun@hust.edu.cn (R. Hu), tao@hust.edu.cn (G. Tao), luoxb@hust.edu.cn (X. Luo).
[1] Run Hu and Jinlin Song contributed equally.

https://doi.org/10.1016/j.nanoen.2020.104687
Received 8 February 2020; Received in revised form 9 March 2020; Accepted 9 March 2020
Available online 12 March 2020

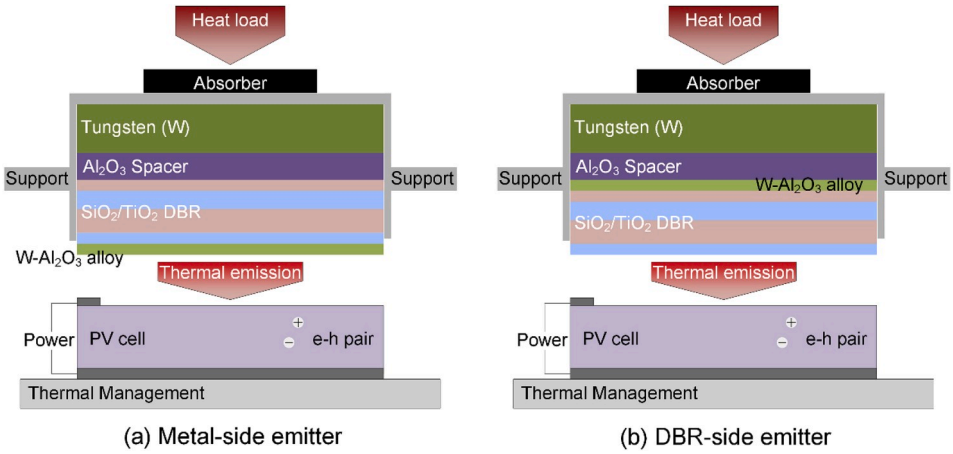

Fig. 1. Schematic of TPV setups with (a) metal-side emitter and (b) DBR-side emitter.

be unnecessary to construct complicated nanostructures to compensate wave vector [28]. TPPs-based emitter, or Tamm emitter for short, has been validated to be adjustable in thermal emission by varying the structures, configurations, dimensions, and materials of the DBR and metal layers [29–32]. Just considering two kinds of materials for the DBR structure, if the total layer number is N, there will be as many as 2^N candidate structures for optimization. Most previous optimization work is only manual optimization with limited cases study, which is far from the optimal structure. Thus, a more advanced and efficient algorithm is demanded to accelerate the optimization. Another challenge is that for TPV system, there are two figure-of-merit parameters, *a.k.a.* the power density P and the system efficiency η, which may be competing during the optimization process. Very recently, Tamm emitter was applied to find the Pareto front of spectral density and spectral efficiency of a TPV [33]. However, their definitions of the spectral density and efficiency are less satisfactory and somewhat unrealistic since they only consider the ideal case without taking a detailed balance analysis of the PV cell into account.

In this paper, we integrate a Tamm emitter and a single-junction GaSb solar cell to construct a TPV system, and take the power density and system efficiency as the coupling parameters to optimize the Tamm emitter based on machine-learning Monte Carlo tree search algorithm [34–36]. Detailed modeling process are introduced and analyzed, and the mechanism is discussed by comparing with manual periodic cases.

2. Theory and methods

2.1. TPV setup

In a typical TPV setup, as shown in Fig. 1, heat load is absorbed by a high-efficiency absorber, enabling more heat can be conducted to the emitter at as high temperature as possible. The absorber is out of our interest here, and usually made of carbon-based materials like carbon nanotubes (CNTs) and soot [13]. An optically thick refractory material like tungsten (W) is used as the mechanical support of the emitter and the heat spreader to generate uniform high temperature of the emitter. Between the optically-thick W and the Tamm structures, a 10-nm aluminum oxide (Al_2O_3) layer acts as the spacer. There are two kinds of structures for Tamm emitters, as shown in Fig. 1, including the metal-side and the DBR-side emitters, and the only difference is the sequence of the DBR and the metal layers. Here, the DBR is consisted of alternative silicon oxide (SiO_2) and titanium oxide (TiO_2) layers at 51 nm and 30 nm, respectively. The metal layer is composed by W–Al_2O_3 alloy with adjustable percentages of W ingredient (f_w). The tailored thermal emission from the Tamm emitter is incident onto the PV cell surface, where the emitted energy above the bandgap energy will be absorbed to generate photocurrent and electricity in the end. The PV cell is cooled by a heat sink, and its temperature is assumed uniformly at 300 K (see Fig. 2).

2.2. Emissivity modelling

To calculate the thermal emission from the Tamm emitter, we first employ the transfer matrix method (TMM) to compute the reflectance spectra, which is convenient to obtain the electromagnetic field distributions [37]. All materials considered are isotropic and nonmagnetic. The tungsten substrate can be regarded as opaque for its enough thickness, so that the spectral emittance can be obtained through the spectral reflectance based on Kirchhoff's law. In TMM, the optical response of each layer (indexed as l = 1, 2, …, N) can be fully described by its relative permittivity. The transfer matrix connects optical responses of different layers, which reads [38].

$$\begin{pmatrix} M_{11} & M_{12} \\ M_{21} & M_{22} \end{pmatrix} = \left[\prod_{l=0}^{N-2} V_{l,l+1} P_{l,l+1} \right] V_{N-1,N}, \tag{1}$$

where the transmission matrix $V_{l,l+1} = \frac{1}{t_{l,l+1}} \begin{bmatrix} 1 & r_{l,l+1} \\ r_{l,l+1} & 1 \end{bmatrix}$ links the amplitudes of the waves at the interfaces of layer l and layer $l+1$, in which $t_{l,l+1}$ and $r_{l,l+1}$ refer to Fresnel's transmission and reflection coefficients at the interface. The propagation matrix of layer l is given by $P_l = \begin{bmatrix} e^{-ik_z d_l} & 0 \\ 0 & e^{ik_z d_l} \end{bmatrix}$ Then, one can obtain the reflectance $R = \rho^2 = \left(\frac{M_{21}}{M_{11}}\right)^2$ with ρ being the reflection coefficient, and meanwhile the electric field distribution $\mathbf{E}(x, z)$ can be solved. Such layer-dependent TMM algorithm is easy to integrated with following machine learning encoding and optimization.

2.3. PV cell modelling

The current density in a PV cell can be calculated as [39–41].

$$J = q(F - R) \tag{2}$$

where q is the elementary charge. F denotes the number flux of photons with energies above the bandgap from the thermal emitter to the PV cell, which can be calculated as

$$F = \int_0^{\lambda_{bg}} \frac{\lambda}{hc} I_{BB}(\lambda) \varepsilon(\lambda) d\lambda \tag{3}$$

where I_{BB} is the blackbody spectral density and $\varepsilon(\lambda)$ is the tailored emissivity spectrum of the Tamm emitter. The Kirchhoff's law is

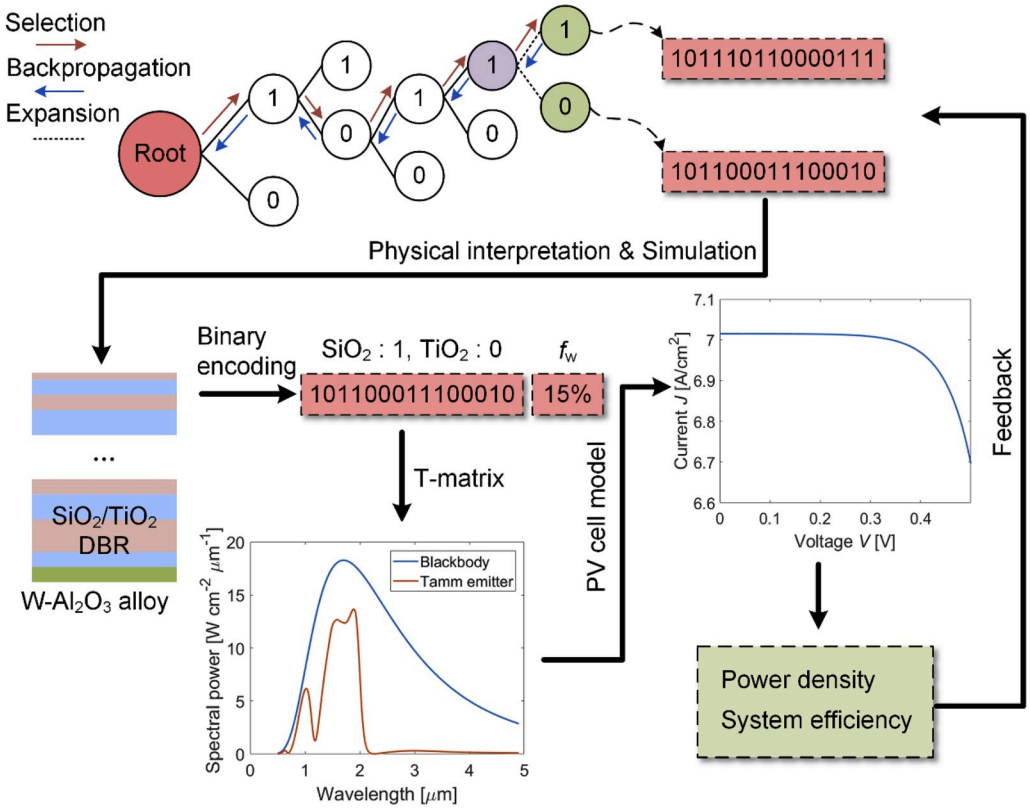

Fig. 2. Schematic of the MCTS optimization process for Tamm emitter, namely the sequence of the DBR layers to maximize the power density and system efficiency of a TPV setup. The MCTS optimization include four steps, i.e. selection, expansion, simulation, and backpropagation. Each sequence of the DBR layers is encoded into binary digits of 1 and 0, and then incorporated into T-matrix algorithm to obtain the emissivity spectrum. Through a PV cell model, the power density and the system efficiency can be obtained for the feedback to the MCTS optimization to predict next digit sequence with larger probability to find the optimal sequence under the framework of machine learning.

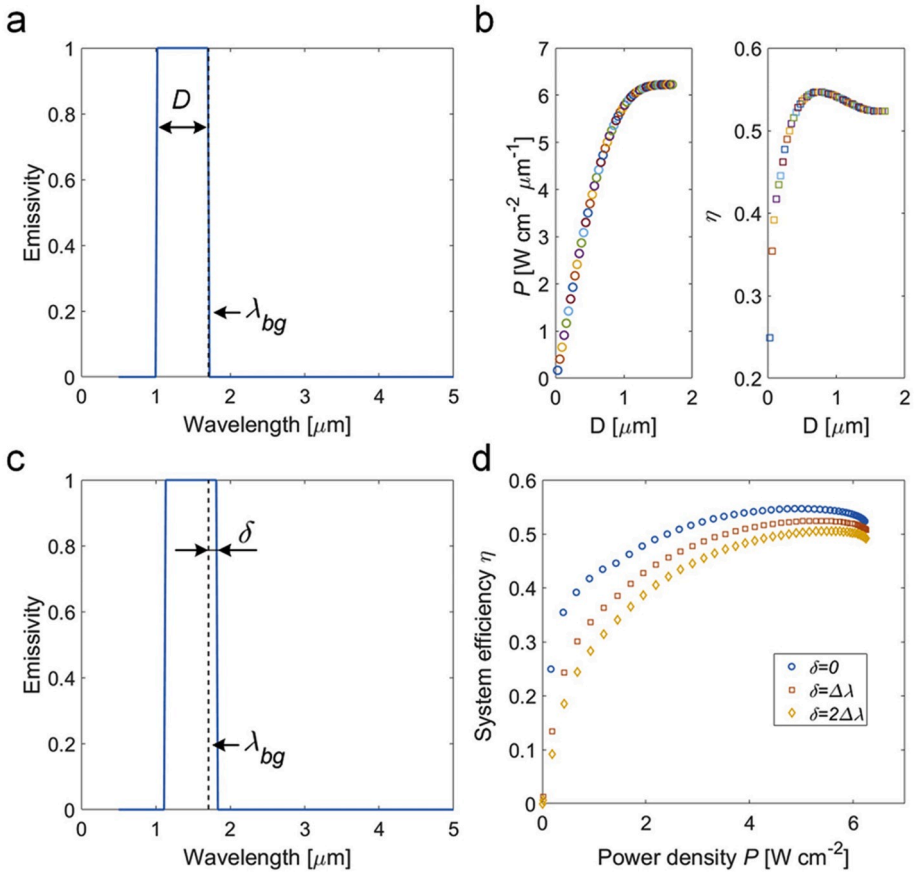

Fig. 3. Ideal emissivity spectrum for the TPV system. (a–b) Discussion on the unity emissivity width D dependence for the power density P and system efficiency η. (c–d) Discussion on the unity emissivity right shift δ dependence for the power density P and system efficiency η.

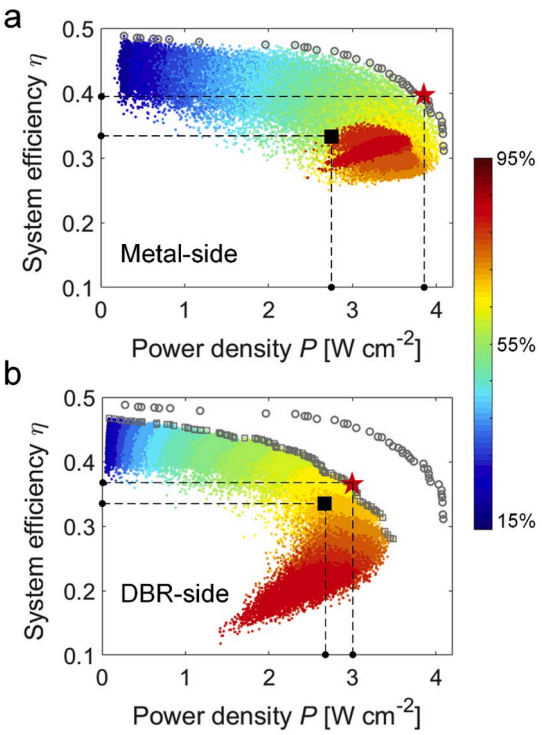

Fig. 4. Optimization results of the (a) metal-side and (b) DBR-side TPV system structures. Red stars denote the optimized structure for both metal- and DBR-side Tamm emitters. Black squares denote the corresponding periodic DBR structures Tamm emitters.

assumed here, thus $\varepsilon(\lambda)$ takes the same value of absorptivity spectrum. $\lambda_{bg} = hc/E_{bg}$ is the wavelength associated with the bandgap, where h and c are the Planck's constant and speed of light respectively. E_{bg} is the bandgap energy, and we assume it as 0.726 eV for GaSb cell, thus the bandgap wavelength λ_{bg} is 1.708 μm. R in Eq. (2) denotes the non-radiative recombination rate inside the cell, which can be modelled as [42,43].

$$R = \left(C_n n + C_p p\right)\left(np - n_i^2\right)t + \frac{1}{\tau}\frac{np - n_i^2}{n + p + 2n_i}t \tag{4}$$

where $n_i = 1.5 \times 10^{12}$ cm^{-3} is the intrinsic carrier concentration. $C_p = C_n = 2.5 \times 10^{30}$ cm^{-6} s^{-1} are the Auger recombination coefficients. τ is the bulk Shockley-Read-Hall (SRH) lifetime. In this work, we assume $\tau =$ 600 ns. t is the thickness of the GaSb cell, and here we assume it as 6 μm n and p are the electron and hole concentrations, depending on the voltage and the doping level. Through these calculations, we can obtain the J-V curve of the PV cell, and the power density as $P = JV$.

As for the system efficiency, we resort to the energy balance analysis. The incident photon energy from the Tamm emitter is

$$P_{in} = \int_0^{\infty} I_{BB}(\lambda)\varepsilon(\lambda)d\lambda \tag{5}$$

among which, the energy portion that can be absorbed by a PV cell is

$$P_{abs} = \int_0^{\lambda_{bg}} \frac{\lambda}{\lambda_{bg}} I_{BB}(\lambda)\varepsilon(\lambda)\eta_{quantum}(\lambda)d\lambda \tag{6}$$

where $\eta_{quantum}$ is the wavelength-dependent quantum efficiency of the GaSb cell. The factor λ/λ_{bg} captures the disadvantage of photons with energy greater than the bandgap energy since the excess energy ($\lambda<\lambda_{bg}$) will not be efficient for photocurrent. The useful power of the PV cell can be calculated as the difference between the absorbed photon energy and the nonradiative energy loss, yielding

$$P_{use} = P_{abs} - P_{loss} = P_{abs} - qVR. \tag{7}$$

Then, the system efficiency can be calculated as $\eta = P_{use}/P_{in}$.

Both the power density P and the system efficiency η are the FOM indexes for the TPVs. A high P is significant to minimize the efficiency loss in the PV cell owing to the loss of open-circuit voltage, while a large η is important to minimizing the thermalization loss. In general, these two parameters can be maximized at different voltage, which means they are kind of competing and a multi-objective Pareto optimization method should be used for tailoring the thermal emission of the Tamm emitter.

2.4. Monte Carlo tree search optimization

To optimize the sequence of DBR layers in both metal-side and DBR-side Tamm emitters, we adopt the Monte Carlo tree search (MCTS) algorithm coupled with Bayesian optimization algorithm in the framework of the python library MDTS (Material Design using Tree Search) [34–36,44,45]. MCTS algorithm is not only suitable for single-objective optimization problem, but also applicable for multi-objective optimization problem. The schematic of the MCTS optimization process used in this work is as shown in Fig. 2. Since here we only consider two kinds of materials, SiO_2 and TiO_2, we use two digits to represent the two materials, i.e. digit 1 for SiO_2 and digit 0 for TiO_2. Any sequence of the digits of 1 and 0 from the root node to the leaf node can be physically interpreted into the specific sequence of SiO_2 and TiO_2 multilayer of DBR structure. Then we integrate the DBR structure into the metal-side or the DBR-side Tamm emitter, and calculate the corresponding emissivity spectrum via the T-matrix algorithm and the power density and system efficiency via the PV cell model. The output of the PV cell model will be feedback to the MCTS algorithm for evaluating the performance of the current binary digit sequence. Each round of MCTS consists of four steps: selection, expansion, simulation and backpropagation. In the selection step, the tree is traversed from the root to a leaf by choosing a child node with the maximum upper confidence bound value. In the expansion step, children nodes are added under the current node. In the simulation step, we obtain and evaluate the output from the PV cell model and store the value as the immediate merit of the corresponding nodes. In the back-propagation step, the visit count of each ancestor node is incremented by one and the cumulative value is also updated to keep consistency. The built-in machine learning process from calculation history can accelerate the prediction of the new-added subtree node with promising possibility to reach the optimal result. When a predetermined calculation number is reached, the best solution so far will be returned. In the real implementation, we also change the W-percentage f_w from 15% to 95% to evaluate the influence of W-percentage on the TPV performance.

3. Results and discussions

3.1. Ideal emissivity spectrum

First, we would like to discuss the ideal emissivity spectrum for TPV system in terms of the width and range of unity emissivity. When the maximum wavelength of unity emissivity is fixed at the bandgap wavelength λ_{bg}, we increase the width D gradually and calculate the corresponding power density P and system efficiency η, as shown in Fig. 3a and 3b. It is seen that with the increase of D, the power density P increases monotonously and tends to a saturation value, while the system efficiency η shows a peak at $D = 0.696$ μm. This is easy to understand that the photons above the bandgap energy (wavelength less than the bandgap wavelength) can be absorbed by the PV cell to separate the electron-hole pair for photocurrent generation. The more photons absorbed, the higher power will be generated, leading to the monotonous trend of width D dependence. While as for the system efficiency, not all absorbed photons will be used for photocurrent generation, and

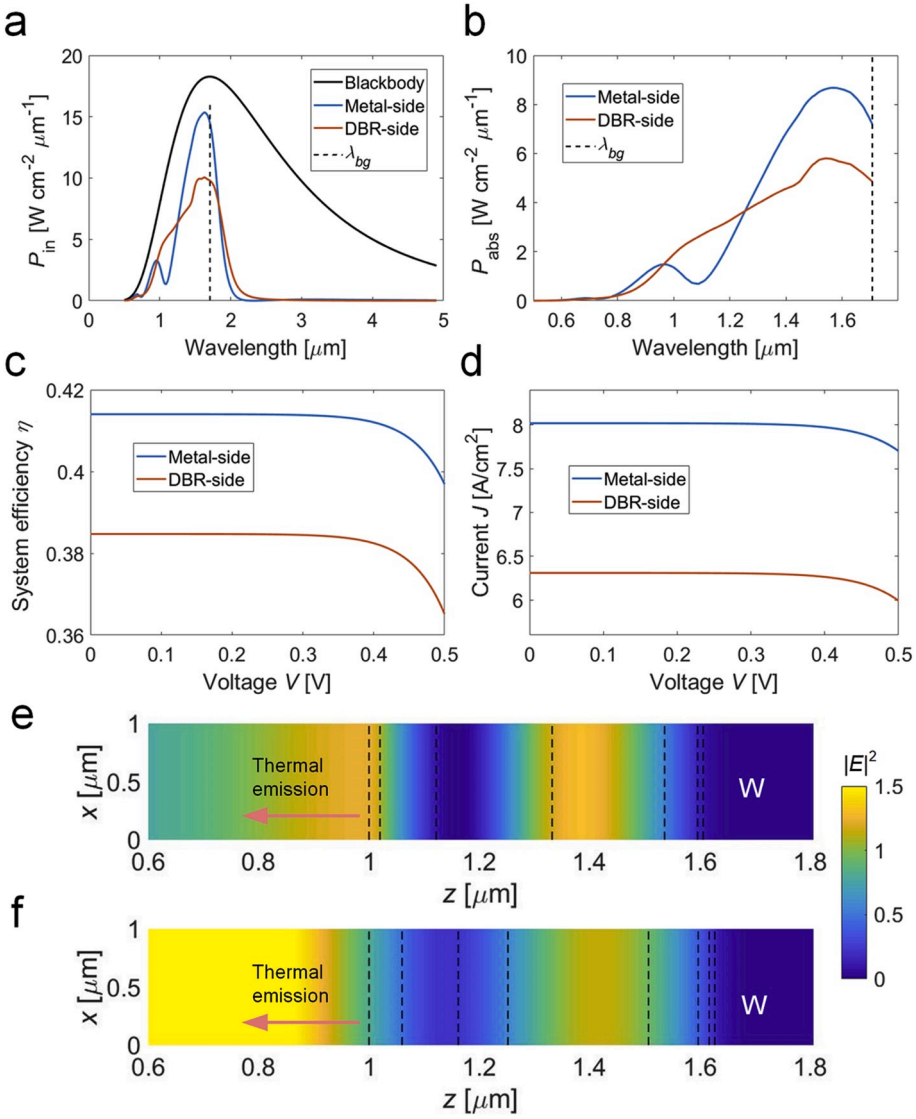

Fig. 5. Comparisons between the metal-side and DBR-side TPV systems. (a–b) Incident and absorbed power spectra comparisons. (c) System efficiency and (d) photocurrent comparisons at different input voltages. Electric field intensity distributions of (e) metal-side and (f) DBR-side emitter at 1.708 μm.

the excess energy will heat up the PV cell with degraded optoelectronic conversion efficiency. These trends have been well understood and agree with previous studies. Then we maintain the width D of the unity emissivity and make fine adjustment on the position by shifting right a small value δ, as shown in Fig. 3c. The corresponding power density and system efficiency are shown in Fig. 3d, from which we can see that even a small right shift $\Delta\lambda = 0.023$ μm leads to a significant drop in both the power density and system efficiency. Note that the ideal emissivity is not easy to achieve, while the practical emissivity spectrum should close to the ideal one as close as possible to maximize the TPV performance.

3.2. Machine-learning optimization results

Then we implement machine-learning MCTS algorithm to maximize the power density and system efficiency of the metal-side and DBR-side Tamm-emitter TPV systems, and the results are shown in Fig. 4. The efficiency of the MCTS algorithm is so high that only less than 1.5% of the total candidates are calculated to achieve the global optimal structure with maximum power density and system efficiency. The color bar denotes the W-percentage f_w in the W–Al_2O_3 alloy from 15% to 95% with 5% as the interval increment. It is seen that both the DBR sequence and the W-percentage f_w influence the optimization, while the latter matters stronger. In both structures, when the f_w is low, the power density is low with a high system efficiency. For the metal-side structure, with the increase of f_w, the power density P increases first and begins to decrease when $f_w > 70\%$. While for the DBR-side structure, similar trends are observed and power density P begins to decrease when $f_w > 80\%$. For higher system efficiency, the f_w should be low; while for high power density, the f_w should be large under the threshold f_w. The Pareto front lines are shown by the gray circles in Fig. 4a and b, and the red star denotes the global optimal ones in both cases. The corresponding binary sequences are 110000000111100 with $f_w = 60\%$ and 001100011111000 with $f_w = 70\%$, respectively, and the corresponding power density and system efficiency are 3.85 W/cm^2 and 39.7% in Figs. 4a, and 3.0 W/cm^2 and 36.5% in Fig. 4b. More importantly, when comparing the Pareto front lines in Fig. 4b, it is obvious that the metal-side structure has higher power density and system efficiency simultaneously than the DBR-side structure.

To quantify the mechanism, we show the detailed comparisons of these two TPV structures in Fig. 5. The incident power spectra from the metal- and DBR-side Tamm emitters are shown in Fig. 5a, both of which are, of course, under the Blackbody emission at the same temperature. It is seen that the spectrum of metal-side emitter has higher intensity near the bandgap wavelength than that of the DBR-side emitter, and more

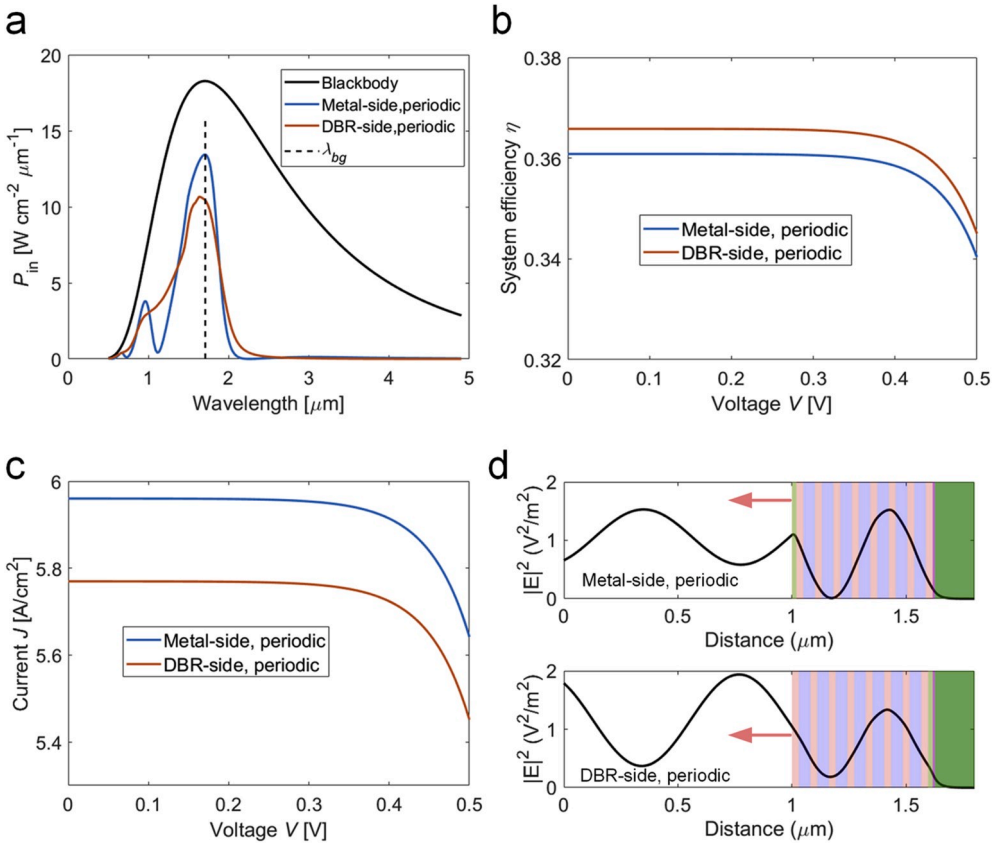

Fig. 6. Comparisons between the metal-side and DBR-side TPV systems with periodic DBR. (a) Incident power spectra comparisons. (b) System efficiency and (c) photocurrent comparisons at different input voltages. (d) Electric field intensity distributions of metal-side and DBR-side emitter with periodic DBR at 1.708 μm.

thermal emission is below the bandgap wavelength. These properties are of great importance for the power density and system efficiency, as discussed in Fig. 3. The corresponding absorbed power spectra are shown Fig. 5b. It is seen that only the thermal photons below the bandgap wavelength can be absorbed by the PV cell, and the metal-side emitter is more efficient to provide desired emission for the PV cell. Other than the power density, the system efficiency and the photocurrent of the metal-side emitter are much higher than the DBR-side emitter at different input voltages. All these details are consistent with the previous optimizations that the metal-side emitter structure is beneficial for the TPV in terms of power density and system efficiency. The electric field distributions of the two optimized structures at 1.708 μm are shown in Fig. 5e and f, respectively. The filled regions are consistent with the material distributions in Fig. 1. The electric fields outside the emitters are typical sine function. Focusing on the inner electric intensity, stronger intensity occurs in the metal-side TPV system compared to that in the DBR-side system, corresponding to stronger thermal emission. Furthermore, to quantitatively discuss the thermal emission, we calculate the local power dissipation density P_{loc} in the dissipation layer with volume V_{loc} (i.e., W and alloy layers), because it is assumed that there is no loss in the rest layers with zero extinction, which is given by $P_{\mathrm{loc}}(x,z) = 0.5\varepsilon_0\omega\iint \mathrm{Im}[\varepsilon(x,z)]|\mathbf{E}(x,z)|^2 dV_{\mathrm{loc}}$ [46], where ε_0 is the vacuum permittivity, ω is the angular frequency, $\mathrm{Im}[\varepsilon(x,z)]$ is the imaginary part of the permittivity. For the metal-side emitter, the majority of thermal emission comes from the alloy layer which reaches 2.8×10^{-3} W/m (W/m^3 for a three-dimensional structure), which is almost 3.8 times larger than that in the DBR-side emitter at the bandgap, which can be used to explain the better performance for the metal-side emitter. Indeed, for standard Tamm emitters, metal film thickness must be optimized to obtain perfect emission in metal-side structures, while a thick metal film behaving as a good reflector is required to have good performance in DBR-side structures. This principle is also applicable for the proposed aperiodic Tamm emitters here, where the thin alloy dissipation layer is not perfectly reflective due to the intrinsic loss [47]. As a result, metal-side emitters usually perform better in this kind of cases. Furthermore, we also compare their TPV performances with the corresponding periodic DBR Tamm emitters. The corresponding binary sequence of the periodic DBR is 010101010101010 with $f_w = 60\%$ and $f_w = 70\%$, respectively for the metal- and DBR-side Tamm emitters.

Similar to Fig. 5, the incident power spectra, system efficiency, the photocurrent, and the electric field distributions of the two periodic-DBR TPV systems are shown in Fig. 6. It is seen that the metal-side Tamm emitters are beneficial to the TPV performance, which is consistent with previous conclusion. The mechanism is also illustrated by the electric field distribution. From the values of incident power spectra, system efficiency, and the photocurrent, it is seen that the machine-learning optimized aperiodic-DBR Tamm emitters are much better for the TPV performance. Such aperiodic DBR cannot be designed by handwork, which is the merit of the present machine learning algorithm for TPV system optimization. Note that the Tamm emitters contains many interfaces, and the interface quality, including the roughness, material defects, thickness accuracy and consistency, will influence the emission intensity, direction, and polarization of thermal emission of the emitter, which consequently affects the performance of TPV system greatly [48,49]. As inspired by our analysis, the material configurations will change the electric field distribution and the thermal emission, thus very precise manufacturing of the experimental samples is of great significance for experimental validation, which should be well designed and optimized in terms of the manufacturing processes and parameters [47,50].

4. Conclusion

In summary, we employ machine learning algorithm to optimize the Tamm emitter structures in TPV system with full considering of the photocurrent generation in the PV cells through the detailed balance analysis. The Pareto front lines of the competing power density and system efficiency are obtained for the metal- and DBR-side Tamm emitters. The ideal emissivity spectrum is initially discussed for both power density and system efficiency first. Then through optimization, the non-trial aperiodic Tamm emitters are obtained and the metal-side one is preferable in terms of the TPV performance. The mechanism is identified by the local power dissipation density and further validated by comparing with the periodic-DBR Tamm emitters. The present machine-learning optimization method is demonstrated to be feasible and efficient, and can be extended for the multi-objective optimization problems in other fields.

Funding

The authors would like to acknowledge the financial support by National Natural Science Foundation of China (51606074, 51625601, 51806070, 51676077), the Ministry of Science and Technology of the People's Republic of China (2017YFE0100600), and the China Post-doctoral Science Foundation (2018M632849).

Declaration of competing interest

The authors declare that they have no known competing financial interests or personal relationships that could have appeared to influence the work reported in this paper.

CRediT authorship contribution statement

Run Hu: Conceptualization, Writing - original draft, Formal analysis, Supervision. **Jinlin Song:** Writing - original draft, Formal analysis. **Guangming Tao:** Supervision, Writing - review & editing. **Xiaobing Luo:** Supervision, Writing - review & editing.

References

[1] S. Fan, Thermal photonics and energy applications, Joule 1 (2) (2017) 264–273.
[2] J. Cuevas, F. García-Vidal, Radiative heat transfer, ACS Photonics 5 (10) (2018) 3896–3915.
[3] Y. Zhai, Y. Ma, S. David, et al., Scalable-manufactured randomized glass-polymer hybrid metamaterial for daytime radiative cooling, Science 355 (6329) (2017) 1062–1066.
[4] H. Bao, C. Yan, B. Wang, et al., Double-layer nanoparticle-based coatings for efficient terrestrial radiative cooling, Sol. Energy Mater. Sol. Cells 168 (2017) 78–84.
[5] R. Hu, S. Huang, M. Wang, et al., Encrypted thermal printing with regionalization transformation, Adv. Mater. 31 (2019) 1807849.
[6] Y. Li, X. Bai, T. Yang, et al., Structured thermal surface for radiative camouflage, Nat. Commun. 9 (1) (2018).
[7] J. Kou, Z. Jurado, Z. Chen, et al., Daytime radiative cooling using near-black infrared emitters, ACS Photonics 4 (2017) 626–630.
[8] R. Hu, S. Zhou, Y. Li, et al., Illusion thermotics, Adv. Mater. 30 (2018) 1707237.
[9] J. Song, S. Huang, Y. Ma, et al., Radiative metasurface for thermal camouflage, illusion and messaging, Optic Express 28 (2) (2020) 875.
[10] E. Carrasco, B. del Rosal, Sanz-Rodrigue, et al., Intratumoral thermal reading during photo-thermal therapy by multifunctional fluorescent nanoparticles, Adv. Funct. Mater. 25 (4) (2015) 615–626.
[11] R. Hu, X. Luo, Two-dimensional phonon engineering triggers microscale thermal functionalities, Nat. Sci. Rev. 6 (2019) 1071–1073.
[12] I. Khodasevych, L. Wang, A. Mitchell, et al., Micro- and nanostructured surfaces for selective solar absorption, Adv. Opt. Mater. 3 (7) (2015) 852–881.
[13] A. Lenert, D. Bierman, Y. Nam, et al., A nanophotonic solar thermophotovoltaic device, Nat. Nanotechnol. 9 (2) (2014) 126–130.
[14] J. Song, L. Lu, B. Li, et al., Thermal routing via near-field radiative heat transfer, Int. J. Heat Mass Tran. 150 (2020) 119346.
[15] S. Huang, J. Zhang, M. Wang, et al., Macroscale thermal diode-like black box with high transient rectificaion ratio, ES Energy Environ. 6 (2019) 51–56.
[16] X. Peng, R. Hu, Macroscale three-dimensional illusion thermotics with separated thermal illusions, ES Energy Environ. 6 (2019) 39–44.
[17] A. Datas, C. Algora, Global optimization of solar thermophotovoltaic systems, Prog. Photovoltaics Res. Appl. (2012) 1040–1055.
[18] H. Seyf, A. Henry, Thermophotovoltaics: a potential pathway to high efficiency concentrated solar power, Energy Environ. Sci. 9 (2016) 2654–2665.
[19] J. Song, M. Si, Q. Cheng, et al., Two-dimensional trilayer grating with a metal/insulator/metal structure as a thermophotovoltaic emitter, Appl. Optic. 55 (6) (2016) 1284.
[20] D. Baranov, Y. Xiao, I. Nechepurenko, et al., Nanophotonic engineering of far-field thermal emitters, Nat. Mater. 18 (9) (2019) 920–930.
[21] J. Song, H. Wu, Q. Cheng, et al., 1D trilayer films grating with W/SiO2/W structure as a wavelength-selective emitter for thermophotovoltaic applications, J. Quant. Spectrosc. Radiat. Transfer 158 (2015) 136–144.
[22] S. Biehs, M. Tschikin, R. Messina, et al., Super-Planckian near-field thermal emission with phonon-polaritonic hyperbolic metamaterials, Appl. Phys. Lett. 102 (13) (2013) 131106.
[23] J. Song, Q. Cheng, Near-field radiative heat transfer between graphene and anisotropic magneto-dielectric hyperbolic metamaterials, Phys. Rev. B 94 (12) (2016) 125419.
[24] Y. Chang, C. Liu, S. Zhang, et al., Realization of mid-infrared graphene hyperbolic metamaterials, Nat. Commun. 7 (1) (2016).
[25] Y. Guo, Z. Jacob, Thermal hyperbolic metamaterials, Optic Express 21 (12) (2013) 15014–15019.
[26] L. Wang, Z. Zhang, Phonon-mediated magnetic polaritonsin the infrared region, Optic Express 19 (6) (2011) A126–A135. Suppl 2.
[27] J. Song, Q. Cheng, Z. Luo, et al., Modulation and splitting of three-body radiative heat flux via graphene/SiC core-shell nanoparticles, Int. J. Heat Mass Tran. 140 (2019) 80–87.
[28] M. Kaliteevski, I. Iorsh, S. Brand, et al., Tamm plasmon-polaritons: possible electromagnetic states at the interface of a metal and a dielectric Bragg mirror, Phys. Rev. B 76 (16) (2007).
[29] Z. Wang, J. Clark, Y. Ho, et al., Narrowband thermal emission realized through the coupling of cavity and Tamm plasmon resonances, ACS Photonics 5 (6) (2018) 2446–2452.
[30] K. Zhou, L. Lu, J. Song, et al., Ultra-narrow-band and highly efficient near-infrared absorption of a graphene-based Tamm plasmon polaritons structure, J. Appl. Phys. 124 (12) (2018) 123102.
[31] Z. Yang, S. Ishii, T. Yokoyama, et al., Tamm plasmon selective thermal emitters, Opt. Lett. 41 (19) (2016) 4453–4456.
[32] H. Zhu, H. Luo, Q. Li, et al., Tunable narrowband mid-infrared thermal emitter with a bilayer cavity enhanced Tamm plasmon, Opt. Lett. 43 (21) (2018) 5230.
[33] N. Jeon, J. Hernandez, D. Rosenmann, et al., Pareto optimal spectrally selective emitters for thermophotovoltaics via weak absorber critical coupling, Adv. Energy Mater. 8 (25) (2018) 1801035.
[34] T. Dieb, S. Ju, J. Shiomi, et al., Monte Carlo tree search for materials design and discovery, MRS Commun. 9 (2) (2019) 532–536.
[35] S. Ju, T. Shiga, L. Feng, et al., Designing nanostructures for phonon transport via Bayesian optimization, Phys. Rev. X 7 (2) (2016), 021024.
[36] M. Yamawaki, M. Ohnishi, S. Ju, et al., Multifunctional structural design of graphene thermoeletrics by Bayesian optimization, Sci. Adv. 4 (6) (2018), eaar4192.
[37] Z.M. Zhang, Nano/microscale Heat Transfer, McGraw-Hill, 2007 xxi, 479.
[38] P. Yeh, Optical Waves in Layered Media, vol. 61, Wiley-Interscience, 2005.
[39] E. Rephaeli, S. Fan, Absorber and emitter for solar thermo-photovoltaic systems to achieve efficiency exceeding the Shockley-Queisser limit, Optic Express 17 (17) (2009) 15145.
[40] K. Chen, T. Xiao, P. Santhanam, et al., High-performance near-field electroluminescent refrigeration device consisting of a GaAs light emitting diode and a Si photovoltaic cell, J. Appl. Phys. 122 (14) (2017) 143104.
[41] K. Chen, P. Santhanam, S. Fan, Suppressing sub-bandgap phonon-polariton heat transfer in near-field thermophotovoltaic devices for waste heat recovery, Appl. Phys. Lett. 107 (9) (2015), 091106.
[42] B. Zhao, K. Chen, S. Buddhiraju, et al., High-performance near-field thermophotovoltaics for waste heat recovery, Nano Energy 41 (2017) 344–350.
[43] X. Liu, Z. Zhang, High-performance electroluminescent refrigeration enabled by photon tunneling, Nano Energy 26 (2016) 353–359.
[44] J. Guo, S. Ju, J. Shiomi, Design of highly-selective radiative-cooling structure accelerated by materials informatics, Opt. Lett. 45 (2) (2020) 343–346.
[45] H. Yamada, C. Liu, S. Wu, Y. Koyama, S. Ju, J. Shiomi, J. Morikawa, R. Yoshida, Predicting materials properties with little data using shotgun transfer learning, ACS Cent. Sci. 5 (10) (2019) 1717–1730.
[46] J. Song, L. Lu, Q. Cheng, Z. Luo, Surface plasmon-enhanced optical absorption in monolayer MoS_2 with one-dimensional Au grating, J. Quant. Spectrosc. Radiat. Transfer 211 (2018) 138–143.
[47] Z. Yang, S. Ishii, T. Yokoyama, T. Dao, M. Sun, P. Pankin, I. Timofeev, T. Nagao, K. Chen, Narrowband wavelength selective thermal emitters by confined Tamm plasmon polaritons, ACS Photonics 4 (2017) 2212–2219.
[48] G. Pühringer, B. Jakoby, Taming parasitic thermal emission by Tamm plasmon polaritons for the mid-infrared, JOSA B 35 (7) (2018) 1490–1503.
[49] S. Guo, A. Sushkov, D. Park, H. Drew, P. Kolb, W. Herman, R. Phaneuf, Impact of interface roughness on the performance of broadband blackbody absorber based on dielectric-metal film multilayers, Optic Express 22 (2) (2014) 1952–1962.
[50] Z. Yang, S. Ishii, T. Yokoyama, T. Dao, M. Sun, T. Nagao, K. Chen, Tamm plasmon selective thermal emitters, Opt. Lett. 41 (19) (2016) 4453–4456.